RSC Advances

PAPER

View Article Online
View Journal | View Issue

Cite this: *RSC Adv.*, 2022, **12**, 12702

Bimetallic CoCu-ZIF material for efficient visible light photocatalytic fuel denitrification

Yi Lu,[ab] Haibo Pan,[ab] Jiafeng Lai,[c] Yuzhou Xia,[c] Lu Chen,[c] Ruowen Liang,*[c] Guiyang Yan*[c] and Renkung Huang*[c]

Effective design of photocatalysts is an effective method to improve the separation of photogenerated carriers, which improves the photocatalytic performance of photocatalysts. In this work, CoCu-ZIF materials with bimetallic structure were synthesized at room temperature for efficient photocatalytic fuel denitrification. The properties and structures of CoCu-ZIF photocatalysts can be effectively controlled by adjusting the molar ratio of cobalt to copper. The as-prepared CoCu-ZIF photocatalysts were characterized by XRD, FT-IR, SEM, TEM, UV-vis, Raman, BET and other techniques. The photoactivity of CoCu-ZIF for the denitrogenation of NCCs has been evaluated using visible light ($\lambda \geq 420$ nm). The results indicate that Co_8Cu_2-ZIF photocatalysts exhibit excellent photocatalytic properties, in which the denitrification rate almost reached 80% after 4 hours under visible light irradiation, which is higher than the degradation ability of ZIF-67 (38%). Transient photoelectrochemical experiments and EIS Nyquist plots indicate that Co_8Cu_2-ZIF with unique structure efficiently improves the separation and transfer of photogenerated electron–hole pairs. Moreover, a possible reaction mechanism was proposed by LC-MS analysis.

Received 17th February 2022
Accepted 19th April 2022

DOI: 10.1039/d2ra01049f

rsc.li/rsc-advances

Introduction

With the rapid development of the world, the human demand for energy is also increasing, especially for low-cost natural energy such as oil, coal and gas.[1,2] However, nitrogen-containing compounds (NCCs) in fuels (gasoline and diesel), such as pyridine and pyrrole, will lead to NO_x emission, reduction of combustion efficiency and increase of CO and particulate emissions during combustion.[3–5] Specifically, NO_x produced by fuel combustion will lead to acid rain, corrode buildings and crops, and change the pH value of soil and rivers.[6] Moreover, NO_x will also seriously impact human health, such as through respiratory diseases and nervous system diseases.[7,8] Therefore, more and more strict environmental regulations have been formulated for the nitrogen content in fuels worldwide.[9,10]

Currently, NCCs in fuel are usually removed by hydrodenitrification (HDN), which consumes expensive hydrogen and requires high temperature (range from 300 to 400 °C) and high-pressure conditions (range from 30 to 130 atmospheres).[11,12] The process is not economical. Photocatalysis technology is a kind of technology with low energy consumption and mild conditions, which has attracted significant attention.[13–15] At present, researchers focus on the use of semiconductor catalysts for photocatalytic removal of NCCs.[16] Although some semiconductors have narrow band gaps and are promising photocatalysts, their photocatalytic efficiency is low due to high recombination rate of photogenerated carriers and low specific surface area.[17] For example, Weineng Hu *et al.* synthesized CdS for the degradation of NCCs in fuel (64%, 4 h)[18] and Bi_2MoO_6 (51%, 4 h).[19] Considering the high specific surface area and excellent photogenerated carrier transport properties, porous nanostructures are deemed to be the key structures of photocatalytic materials.[20]

Metal–organic framework materials (MOFs) have the characteristics of high specific surface area, regular pore structure, good chemical stability and convenient synthesis,[21,22] so they are widely used in adsorption and separation,[23] gas storage, catalytic reaction (including chemical catalysis,[24,25] electrocatalysis[26,27] and photocatalysis,[28] sensors,[29] electronic or optical devices[29] and so on). Meanwhile, the high specific surface area of MOFs can also improve the adsorption of target pollutants and increase the number of active sites,[30,31] which has obvious application potential to improve the photocatalytic performance of semiconductors. Furthermore, compared with traditional inorganic semiconductors, it is noteworthy that the structures and functionalities of MOFs can be readily tuned *via* the modification of their organic linkers or metal centers.[32] ZIFs are excellent photocatalytic material, which has been applied in many fields.[33,34] For example, ZIF-67 (Co) is a typical Co-based ZIF with high pore volume and specific surface area.[35] Changli

[a]*College of Chemistry, Fuzhou University, Fuzhou, Fujian 350116, P. R. China*
[b]*Fujian Key Lab of Medical Instrument and Pharmaceutical Technology, Fuzhou University, Fuzhou, Fujian 350108, P. R. China*
[c]*Fujian Provincial Key Laboratory of Featured Materials in Biochemical Industry, Ningde Normal University, Ningde 352100, China. E-mail: t1432@ndnu.edu.cn*

Shi *et al.*[36] synthesized Ag/ZIF-67/TiO_2/Cu sheet, which displayed greatly enhanced photocatalytic activity for the degradation of 4-ATP (~100%, 15 min). Interestingly, the catalyst containing copper has strong adsorption for nitrogen-containing compounds. Yang Xu *et al.*[37] synthesised 3% CuO/NaY zeolite that could adsorb 75 percent of N-nitropyrrolidine (NPYR). However, single metal ZIF (Cu) are harder to synthesize. At present the modification of metal elements of ZIFs has become a research hotspot, hoping to make up for the defects of single metal ZIFs.[38,39] Bimetallic ZIFs can optimize the energy conversion mechanism by virtue of the synergy between bimetallic elements. Herein, CoCu bimetallic ZIF was prepared by introducing Cu and used for photocatalytic fuel denitrification. Compared with ZIF-67, the prepared CoCu bimetallic ZIF showed excellent photocatalytic fuel denitrification activity. In this study, bimetallic ZIF was used as photocatalytic fuel denitrification catalyst for the first time.

Experimental

Materials and reagents

Cobalt nitrate hexahydrate [$Co(NO_3)_2 \cdot 6H_2O$], copper nitrate trihydrate [$Cu(NO_3)_2 \cdot 3H_2O$], cetyltrimethylammonium bromide (CTAB), pyridine and octane were supplied by Aladdin Reagent Co., Ltd. All chemical reagents are of analytical grade and used as received.

Synthesis of CoCu-ZIF

In a typical synthetic procedure, 2-methylimidazole (4.105 g, 50 mmol) was dissolved in 70 mL distilled (DI) water. While $Co(NO_3)_2 \cdot 6H_2O$ (232.8 mg, 0.8 mmol), $Cu(NO_3)_2 \cdot 3H_2O$ (48.3 mg, 0.2 mmol) and CTAB (7.5 mg, 0.02 mmol) were dissolved in 10 mL DI water. Then the two solutions were mixed and kept at room temperature for 24 h after stirring for 1 h. The final sample was collected by centrifugation at 10 000 rpm for 10 min, washed several times with ethanol, and dried under vacuum at 60 °C for 12 h. The obtained sample was Co_8Cu_2-ZIF.

Changing the molar ratio of cobalt to copper, we can get ZIF-67 (10 : 0), Co_9Cu_1-ZIF (9 : 1), Co_7Cu_3-ZIF (7 : 3), Co_6Cu_4-ZIF (6 : 4), Co_5Cu_5-ZIF (5 : 5), respectively.

Characterizations

X-ray diffraction (XRD) patterns were obtained using a Bruker D8 Advance X-ray diffractometer. Fourier-transform infrared reflectance (FT-IR) spectra were measured using a Shimadzu irprestige-21 spectrophotometer. The morphology of the prepared samples was evaluated using a TESCAN MIRA4 field emission scanning electron microscopy (SEM) instrument, Tecnai G2 F20 S-TWIN (FEI) transmission electron microscopy (TEM) apparatus. The X-ray photoelectron spectroscopy (XPS) profiles of the samples were obtained using a Thermo Scientific K-Alpha instrument equipped with a monochromatic Al Lα X-ray source. The UV-Vis diffuse reflectance spectra (DRS) of the samples were obtained using a Shimadzu UV-2700 ultraviolet-visible-near-infrared spectrophotometer over the wavelength range of 250–800 nm. High-performance liquid chromatography-mass spectrometry (HPLC-MS) experiments were performed using an Agilent 1200 series system, equipped with an Agilent Zorbax Eclipse XDB-C18 column (2.1 mm × 100 mm × 3.5 m). Photocurrent measurements were conducted using a BAS Epsilon workstation. Electrochemical impedance spectroscopy (EIS) experiments were conducted using a Precision PARC workstation.

Photocatalytic activity measurements

First, 100 μg g^{-1} simulated NCCs-containing gasoline fuel was prepared by dissolving 70 mg pyridine in 1.0 L octane. Then, 50 mg photocatalyst and 50 mL pyridine/octane solution (100 μg g^{-1}) were added into a quartz reactor. The suspension was stirred in the dark for 1.5 h to ensure the adsorption–desorption equilibrium was reached. Afterward, the suspensions were irradiated using a 300 W Xe lamp (PLS-SXE 300) equipped with a UV-cut filter to cut off light of wavelength shorter than 420 nm. At selected time intervals, aliquots of the suspension were removed and centrifuged. The residual concentration of pyridine in the supernatant was monitored using a Varian Cary 60 spectrometer.

Results and discussion

Structural and morphological characterization

XRD analysis was used to determine the crystal structures of the as-prepared samples. The XRD patterns of photocatalysts with different molar ratio of CoCu-ZIFs were shown in Fig. 1(a). The characteristic peaks of prepared ZIF-67 appeared at 7.3°, 10.4°, 12.7°, 18.0°, 22.1°, 24.6°, 26.7° could be attributed to the (011), (002), (112), (222), (114), (233) and (134) reflections were identified with simulated ZIF-67.[40] In addition, the XRD pattern of CoCu-ZIFs are similar to that of ZIF-67, which indicated that the addition of copper had almost no effect on crystallinity. However, one can see that the characteristic peaks show systematic shifts toward low angles as an increase in the copper content in CoCu-ZIFs, see Fig. 1(b), consistent with the fact that the ionic radius of Co^{2+} is larger than that of Cu^{2+}.[41]

The structures and chemical bonds of different samples were studied by Fourier transform infrared spectroscopy (FT-IR). The peaks were primarily attributed to the 2-methylimidazole ligand. As is illustrated in Fig. 2, for the $Co_{10}Cu_0$-ZIF (ZIF-67), the peaks ranging from 600–1500 cm^{-1} were due to the stretching and bending of the imidazole group. A minor peak at

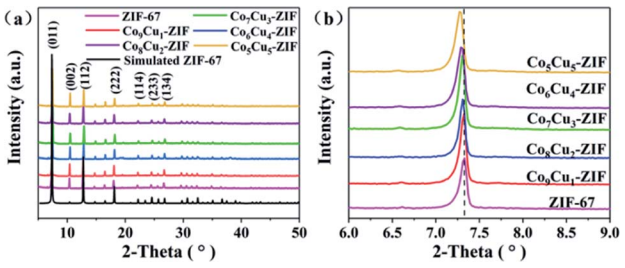

Fig. 1 X-ray diffraction patterns of ZIF-67 and CoCu-ZIFs (a), and the enlarged regions of the XRD patterns (b).

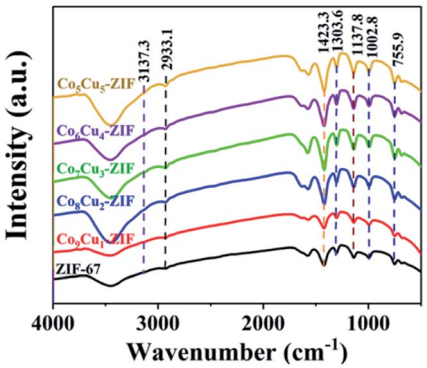

Fig. 2 FT-IR pattern of CoCu-ZIFs and ZIF-67.

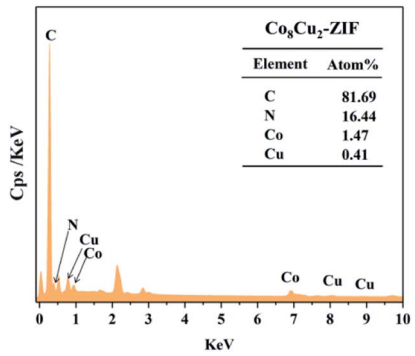

Fig. 4 EDS spectrum of Co_8Cu_2-ZIF.

1423.3 cm^{-1} was owing to the stretching mode of C=N bonding in 2-MIM. The peaks obtained at 2933.1 and 3137.3 cm^{-1} were attributed to the stretching of C–H from the aliphatic methyl group and aromatic ring of 2-MIM, respectively. The positions of peaks correspond well with the published report.[42] As expected, the composite CoCu-ZIFs contain all the chemical bonds belong to ZIF-67. The result further confirmed the successful preparation of CoCu-ZIFs and maintained the structure integrity of ZIF-67 in this composite.[43]

The morphologies and structures of CoCu-ZIFs and ZIF-67 were characterized using SEM and TEM. The SEM images of CoCu-ZIFs and ZIF-67 (Fig. 3(a)–(f)) shows dispersed and uniform cubic morphology with an average diameter of 450 nm and a smooth surface. Furthermore, with the increase of copper content, there were not many discernible differences in morphology. The EDS spectrums (Fig. 4) verify the presence of elements N, C, Co, Cu in bimetal CuCo-ZIF.

To obtain further information about the microstructure of the CoCu-ZIF composite, TEM analyses were performed. As shown in Fig. 5, the introduction of Cu(II) has no significant impact on the morphology of ZIF-67. The EDS elemental mapping indicates the equal distribution of Cu, Co, C and N in the CoCo-ZIF. What's more, copper is randomly substituted for cobalt to ensure the uniformity and stability of the CoCu-ZIF.

In order to further explore the specific surface area and pore size distribution, nitrogen adsorption/desorption experiments were carried out. The N_2 adsorption/desorption isotherms of CoCu-ZIFs samples are shown in Fig. 6. The corresponding BET specific surface areas and pore volumes are summarized in Table 1. As shown in Fig. 6(a), ZIF-67 and Co_8Cu_2-ZIF belonged to I type adsorption behaviour. The BET surface areas for the

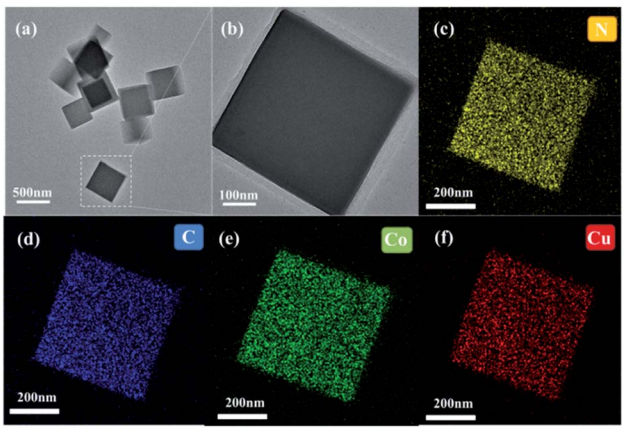

Fig. 5 Transmission electron microscopy images of (a and b) Co_8Cu_2-ZIF, and (c–f) EDS mapping of Co_8Cu_2-ZIF.

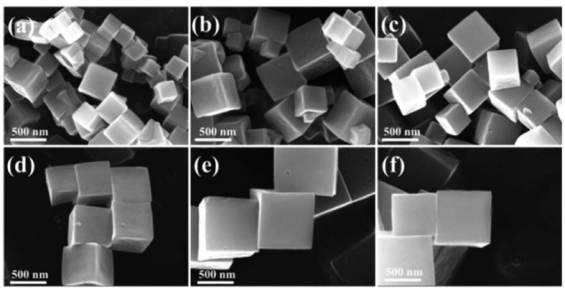

Fig. 3 SEM images of (a) ZIF-67, (b) Co_9Cu_1-ZIF, (c) Co_8Cu_2-ZIF, (d) Co_7Cu_3-ZIF, (e) Co_6Cu_4-ZIF, (f) Co_5Cu_5-ZIF.

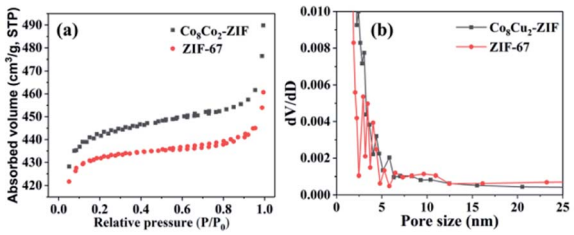

Fig. 6 (a) N_2 adsorption/desorption isotherms distribution curves and (b) pore size distribution curves of Co_8Cu_2-ZIF and ZIF-67.

Table 1 BET surface areas and pore volumes of Co_8Cu_2-ZIF and ZIF-67

Sample	BET surface area (m^2 g^{-1})	Pore volume (cm^3 g^{-1})
Co_8Cu_2-ZIF	1834.71	0.788
ZIF-67	1493.24	0.713

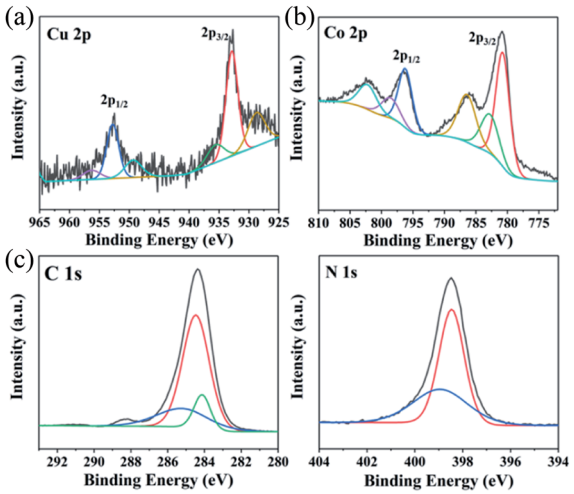

Fig. 7 High resolution XPS spectra of (a) Cu 2p, (b) Co 2p, (c) C 1s, and N 1s for Co_8Cu_2-ZIF.

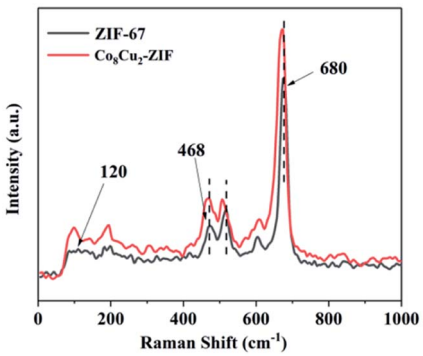

Fig. 8 Raman spectra of ZIF-67 and Co_8Cu_2-ZIF.

ZIF-67 and Co_8Cu_2-ZIF are 1493.24 $m^2\ g^{-1}$ and 1834.71 $m^2\ g^{-1}$, respectively (Table 1). Obviously, The BET surface area of Co_8Cu_2-ZIF is larger than that of ZIF-67. A high BET surface area might be beneficial for providing more active sites, hence could lead to enhanced photocatalytic performance.[27,44] From the corresponding pore size distributions of Fig. 6(b), more mesopores with increased pore sizes are generated with the introduction of Cu.

XPS measurements were used to determine the elements and valence states of Co_8Cu_2-ZIF. To get clearer information, the high-resolution XPS spectra analysis was carried out. The Cu 2p's high-resolution XPS spectrum is shown in Fig. 7(a). It can be realized that peaks centered at 932.51 eV was related to Cu $2p_{3/2}$ and peak at 953.71 eV was related to Cu $2p_{1/2}$ of Cu(II). Fig. 7(b) was the high-resolution XPS spectrum extracted from Co 2p. The main two peaks were centered at 779.01 eV and 796.31 eV, which can be appointed to the binding energies of $2p_{3/2}$ and $2p_{1/2}$ of Co(II). As can be seen from the high-resolution spectrum of C 1s in Fig. 7(c), peaks centered at 284.1 and 284.58 are attributed to C–C and C–N bonds in CuCo-ZIF. Also, the

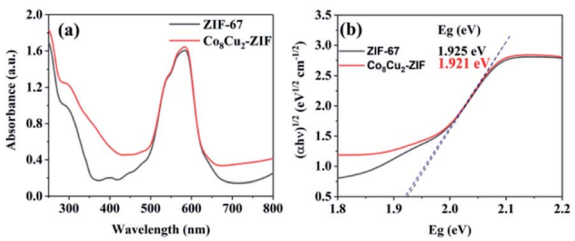

Fig. 9 UV-vis DRS spectra (a) and energy band gaps (E_g) (b) of samples.

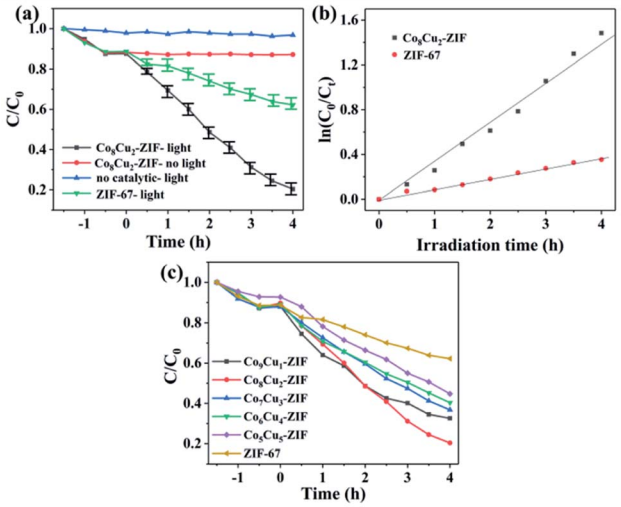

Fig. 10 (a) Photocatalytic denitrogenation of pyridine under different conditions, (b) kinetics of photocatalytic denitrogenation of pyridine over Co_8Cu_2-ZIF and ZIF-67, (c) photocatalytic denitrogenation of pyridine over CoCu-ZIFs.

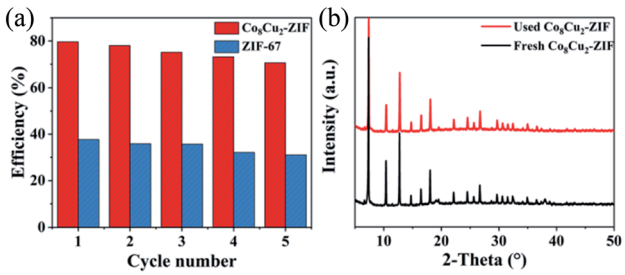

Fig. 11 (a) Cycling experiments of photocatalytic denitrogenation of pyridine over Co_8Cu_2-ZIF, (b) XRD patterns of fresh Co_8Cu_2-ZIF and used Co_8Cu_2-ZIF recovered after five cycles of photocatalysis.

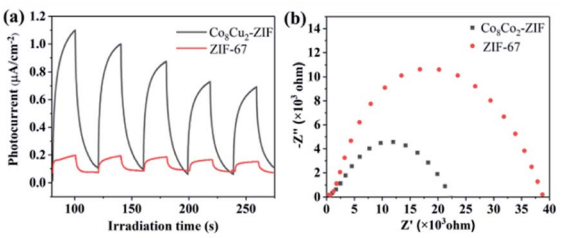

Fig. 12 (a) Nyquist impedance plots of Co_8Cu_2-ZIFs and ZIF-67, (b) transient photocurrent responses of Co_8Cu_2ZIFs and ZIF-67 using visible light ($\lambda \geq 420$ nm).

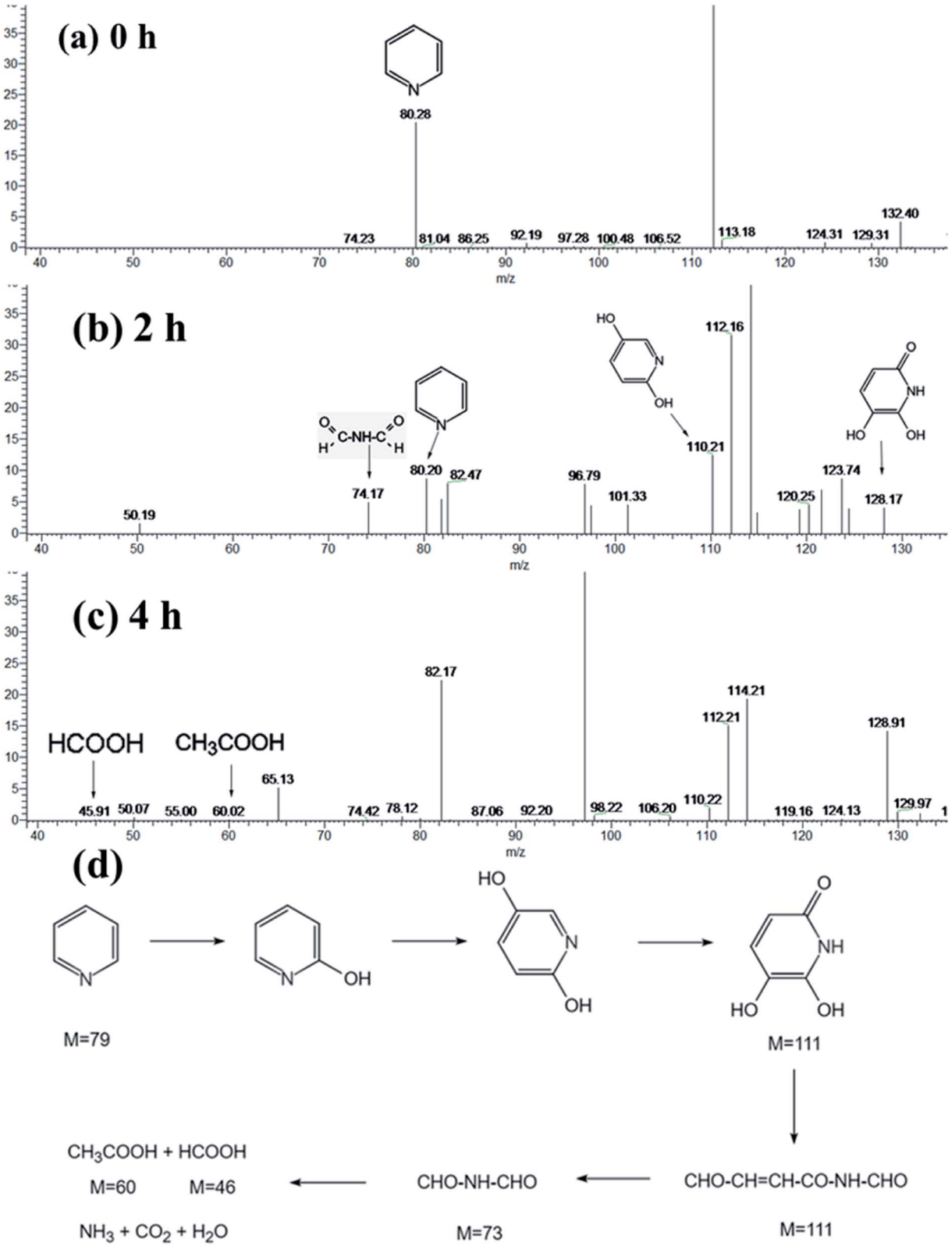

Fig. 13 High-performance liquid chromatography-MS profiles of pyridine after different irradiation times: (a) 0, (b) 2 h and (c) 4 h, and (d) possible denitrogenation pathway of pyridine.

peak located at 298.48 represented the tertiary N bonded to carbon atoms.[45] These results further proved that the chemical component of as-fabricated products was CuCo-ZIF.

The structure samples were further investigated by Raman spectrum, as shown in Fig. 8. A peak can be observed in the Raman shift region at 120 cm^{-1}, which can be attributed to

cobalt ions of ZIF-67.[46] The peaks at 468, 680 cm^{-1} were associated to ZIF-67, which vibrational mode of the 2-methylimidazolate ligand at 680 cm^{-1} and Co–N bond at 468 cm^{-1}.[47] It was noticeable that some peaks of Co_8Cu_2-ZIF were shifted comparing to the ZIF-67.[48] The spectrum of Co_8Cu_2-ZIF is similar to ZIF-67's, further proving the good retention of ZIF-67 structure in the Co_8Cu_2-ZIF.

UV-Vis DRS spectra suggested that all CoCu-ZIF samples exhibited strong visible light absorption (Fig. 9). The band gap energies of the photocatalysts in this study were calculated using the Kubelka–Munk formula: $\alpha h\nu = A(h\nu - E_g)\eta/2$, where α, h, ν, A, and E_g are the absorption coefficient, the Planck constant, the frequency of light, a constant, and the absorption band gap energy, respectively. The value of η depends on the optical transition type of the semiconductor photocatalyst, and $\eta = 1$ for the systems in our study because ZIF-67 is indirect band gap semiconductor.[45] The introduction of copper changed the sample from purple to blue purple. The approximative band gaps of ZIF-67, Co_8Cu_2-ZIF were 1.925 eV and 1.921 eV. The band gap decreased as the content of copper increased, The reduction of the band gap of CoCu-ZIF can be attributed to the formation of a new energy level in the band structure of CoCu-ZIF since chemical bonds between ZIF-67(Co) and Cu(II) may have created.[49]

Photocatalytic performance

The photoactivity of CoCu-ZIF for the denitrogenation of NCCs have been evaluated using visible light ($\lambda \geq 420$ nm). As illustrated in Fig. 10, Co_8Cu_2-ZIF exhibited excellent catalytic performance (80%), however, there is rarely catalytic activity without light. Fig. 9(a) also displayed the comparison of the pyridine denitrogenation efficiencies of Co_8Cu_2-ZIF (80%) and ZIF-67 (38%). The reaction kinetics data for the pyridine photo–denitrogenation reaction are displayed in Fig. 9(b). The rate constants of Co_8Cu_2-ZIF and ZIF-67 were calculated to be 0.348 and 0.091 h^{-1}, respectively. Sample Co_8Cu_2-ZIF presented the highest photoactivity. Significantly, the rate constant of Co_8Cu_2-ZIF was 3.82 times higher than ZIF-67. Fig. 9(c) shows photocatalytic denitrogenation of pyridine over CoCu-ZIFs, Co_8Cu_2-ZIF has the best photoactivity, obviously. The higher photoactivity of Co_8Cu_2-ZIF could be attributed to: (i) The introduction of copper improves the utilization of light; (ii) Compared with ZIF-67, Co_8Cu_2-ZIF has larger specific surface area, exposes more active sites and reduces carrier recombination; (iii) Appropriate copper cobalt ratio is conducive to synergistic effect.

The stability and recyclability of catalyst

To study the stability of Co_8Cu_2-ZIF, the cycling test was conducted in five consecutive runs (Fig. 11(a)). The denitrogenation efficiencies after 5 run still was 71%, with slightly decreasing of 9%. The insignificant reduction of catalytic activity is a common phenomenon during cycling tests, which may be due to the leaching and poisoning of active constituent in catalysts.[50] Notably, the Co_8Cu_2-ZIF still remained relatively high catalytic activity after five consecutive runs, suggesting this material may be suitable for industrial use. Furthermore, the XRD patterns of the fresh and used Co_8Cu_2-ZIF composites are illustrated in Fig. 11(b). The XRD results revealed that the characteristic peaks of the Co_8Cu_2-ZIF composites did not exhibit any significant changes after five cycles.

Photocatalytic mechanism

To further appraise the separation efficiency of the photogenerated electron–hole pairs, transient photoelectrochemical experiments were performed. As shown in Fig. 12(a), the photocurrent density of Co_8Cu_2-ZIF was significantly higher than ZIF-67 under the experimental conditions in this study, during five on–off cycles, which indicated that Co_8Cu_2-ZIF presented lower photogenerated electron–hole recombination rate and higher electron transport than ZIF-67.[51] While photocurrent decay attributable to photo-corrosion can be observed during five on–off cycles. It may be caused by the leaching of some metal ions.[52] Moreover, to better understand the excellent charge carrier transmission performance of Co_8Cu_2-ZIF, EIS Nyquist plots have been obtained (Fig. 12(b)). The Nyquist plot radius of Co_8Cu_2-ZIF was smaller than ZIF-67, which revealed that Co_8Cu_2-ZIF exhibited better separation of its electron–hole pairs and more photogenerated charge carries than ZIF-67, and, consequently, it presented higher photocatalytic fuel denitrification performance.[53,54]

The HPLC-MS spectrometry results are displayed in Fig. 13(a)–(c). Upon irradiation for 240 min, the peak intensity of pyridine at approximately $m/z = 80.28$ was greatly decreased, compared Fig. 13(a) and (c), which implied the successful denitrogenation of pyridine. At the same time, two new peaks at $m/z = 74.17$, and 112.16 gradually appeared (Fig. 13(b)), which suggested that pyridine has been transformed into C_2H_2ONH and $C_5H_5O_2N$, which are protonated intermediate products. Furthermore, the possible denitrogenation pathway of pyridine is illustrated in Fig. 13(d)

Conclusion

Containing copper doped CoCu-ZIFs can be obtained by solvent method at room temperature. CoCu-ZIFs still maintain uniform cube morphology. Ultraviolet-visible spectra supported that Co_8Cu_2-ZIF samples presented greater light-harvesting ability than ZIF-67 in the visible light. What's more, compared to the ZIF-67, the Co_8Cu_2-ZIF sample presented significantly higher performance for the photocatalytic denitrogenation of pyridine (~80%, 4 h) using visible light ($\lambda \geq 420$ nm), which was beneficial for the separation and transfer of the photogenerated electron–hole pairs and absorption of light. Due to the fact that the atomic radius of copper is similar to that of cobalt and dispersion uniformity of copper in CoCu-ZIF, the Co_8Cu_2-ZIF sample also displayed excellent stability and reproducibility. Under the catalysis of Co_8Cu_2-ZIF, pyridine was finally transformed into harmless small molecules. At last, this work could provide a strategy toward the design of low-cost, highly efficient photocatalytic fuel denitrification using ZIFs as promising precursors.

Conflicts of interest

There are no conflicts to declare.

Acknowledgements

This work was financially supported by program for National Natural Science Foundation of China (21806085, 22108129), Innovative Research Team in Science and Technology in Fujian Province University, Natural Science Foundation of Fujian Province (2019J05121, 2019J01837, 2021J05253), Research Project of Ningde Normal University (No. 2019T03, 2020FZ08, 2020T01).

References

1 S. Delpachitra, K. Hou and S. Cottrell, *Energy Econ.*, 2020, **91**, 104846.
2 A. Díaz, G. A. Marrero, L. A. Puch and J. Rodríguez, *Energy Econ.*, 2019, **81**, 1056–1077.
3 L. Wang, D. Xie, Y. Ma, M. Sun, N. Mominou, W. Jiang, C. Shufeng and C. Jing, *Fuel Process. Technol.*, 2021, **216**, 106802.
4 S. Albersberger, J. Hein, M. W. Schreiber, S. Guerra, J. Han, O. Y. Gutiérrez and J. A. Lercher, *Catal. Today*, 2017, **297**, 344–355.
5 R. D. Deese, R. E. Morris, A. E. Metz, K. M. Myers, K. Johnson and T. N. Loegel, *Energy Fuels*, 2019, **33**, 6659–6669.
6 V. A. Kirillov, E. I. Smirnov, Y. I. Amosov, A. S. Bobrin, V. D. Belyaev and V. A. Sobyanin, *Kinet. Catal.*, 2009, **50**, 18–25.
7 N. E. Paucar, P. Kiggins, B. Blad, K. De Jesus, F. Afrin, S. Pashikanti and K. Sharma, *Environ. Chem. Lett.*, 2021, **19**, 1205–1228.
8 M. R. Jury, *Atmos. Pollut. Res.*, 2020, **11**, 1226–1237.
9 C. Yin, *Environ. Impact Assess. Rev.*, 2021, **88**, 106551.
10 Y. Han, S. Hu, Y. Sun, X. Sun, M. Tan, Y. Xu, J. Tian, R. Li and Z. Shao, *Energy Fuels*, 2018, **32**, 5072–5080.
11 S. S. Bello, C. Wang, M. Zhang, H. Gao, Z. Han, L. Shi, F. Su and G. Xu, *Energy Fuels*, 2021, **35**, 10998–11016.
12 S. Badoga, P. Misra, G. Kamath, Y. Zheng and A. Dalai, *Catalysts*, 2018, **8**, 645.
13 H. Luo, Z. Zeng, G. Zeng, C. Zhang, R. Xiao, D. Huang, C. Lai, M. Cheng, W. Wang, W. Xiong, Y. Yang, L. Qin, C. Zhou, H. Wang, Y. Zhou and S. Tian, *Chem. Eng. J.*, 2020, **383**, 123196.
14 Y. Qian, F. Zhang and H. Pang, *Adv. Funct. Mater.*, 2021, **31**, 2104231.
15 V. N. Rao, N. L. Reddy, M. M. Kumari, K. K. Cheralathan, P. Ravi, M. Sathish, B. Neppolian, K. R. Reddy, N. P. Shetti, P. Prathap, T. M. Aminabhavi and M. V. Shankar, *J. Environ. Manage.*, 2019, **248**, 109246.
16 R. Huang, R. Liang, H. Fan, S. Ying, L. Wu, X. Wang and G. Yan, *Sci. Rep.*, 2017, **7**, 7858.
17 W. Zhan, L. Sun and X. Han, *Nano-Micro Lett.*, 2019, **11**, 1.
18 W. Hu, M. Jiang, R. Liang, R. Huang, Y. Xia, Z. Liang and G. Yan, *Dalton Trans.*, 2021, **50**, 2596–2605.
19 W. Hu, G. Yan, R. Liang, M. Jiang, R. Huang, Y. Xia, L. Chen and Y. Lu, *RSC Adv.*, 2021, **11**, 23288–23300.
20 X. Zhang, C. Li, J. Liang, J. Wang, J. Zhang, X. Chen, F. Wang and R. Li, *ChemCatChem*, 2020, **12**, 1212–1219.
21 R. Liang, F. Jing, L. Shen, N. Qin and L. Wu, *Nano Res.*, 2015, **8**, 3237–3249.
22 J. Meng, X. Liu, C. Niu, Q. Pang, J. Li, F. Liu, Z. Liu and L. Mai, *Chem. Soc. Rev.*, 2020, **49**, 3142–3186.
23 M. Davoodi, F. Davar, M. R. Rezayat, M. T. Jafari, M. Bazarganipour and A. E. Shalan, *RSC Adv.*, 2021, **11**, 13245–13255.
24 R. Liang, Z. Liang, F. Chen and L. Wu, *Chin. J. Catal.*, 2020, **41**, 188–199.
25 R. Liang, F. Jing, G. Yan and L. Wu, *Appl. Catal., B*, 2017, **218**, 452–459.
26 M. Ying, R. Tang, W. Yang, W. Liang, G. Yang, H. Pan, X. Liao and J. Huang, *ACS Appl. Nano Mater.*, 2021, **4**, 1967–1975.
27 D. Feng, Y. Cheng, J. He, L. Zheng, D. Shao, W. Wang, W. Wang, F. Lu, H. Dong, H. Liu, R. Zheng and H. Liu, *Carbon*, 2017, **125**, 454–463.
28 T. Xia, Y. Lin, W. Li and M. Ju, *Chin. Chem. Lett.*, 2021, **32**, 2975–2984.
29 P. Gao, R. Liu, H. Huang, X. Jia and H. Pan, *RSC Adv.*, 2016, **6**, 94699–94705.
30 Y. Li, K. Zhou, M. He and J. Yao, *Microporous Mesoporous Mater.*, 2016, **234**, 287–292.
31 B. Luan Tran, H.-Y. Chin, B. K. Chang and A. S. T. Chiang, *Microporous Mesoporous Mater.*, 2019, **277**, 149–153.
32 J. Qiu, X. Zhang, Y. Feng, X. Zhang, H. Wang and J. Yao, *Appl. Catal., B*, 2018, **231**, 317–342.
33 N. Cheng, L. Ren, X. Xu, Y. Du and S. X. Dou, *Adv. Energy Mater.*, 2018, **8**, 1801257.
34 P. Kukkar, K.-H. Kim, D. Kukkar and P. Singh, *Coord. Chem. Rev.*, 2021, **446**, 214109.
35 G. Zhong, D. Liu and J. Zhang, *J. Mater. Chem. A*, 2018, **6**, 1887–1899.
36 C. Shi, L. Qin, S. Wu, S.-Z. Kang and X. Li, *Chem. Eng. J.*, 2021, **422**, 129970.
37 Y. Xu, H.-d. Liu, J. H. Zhu, Z.-y. Yun, J.-h. Xu, Y. Cao and Y.-l. Wei, *New J. Chem.*, 2004, **28**, 244.
38 M. A. Mohamud and A. B. Yurtcan, *Int. J. Hydrogen Energy*, 2021, **46**, 33782–33800.
39 H. Gao, J. Zang, X. Liu, Y. Wang, P. Tian, S. Zhou, S. Song, P. Chen and W. Li, *Appl. Surf. Sci.*, 2019, **494**, 101–110.
40 X. Wang, L. Yu, B. Y. Guan, S. Song and X. W. D. Lou, *Adv. Mater.*, 2018, e1801211, DOI: **10.1002/adma.201801211**.
41 R. D. Shannon, *Acta Crystallogr., Sect. A: Cryst. Phys., Diffr., Theor. Gen. Crystallogr.*, 1976, **32**, 751–767.
42 A. Khan, M. Ali, A. Ilyas, P. Naik, I. F. J. Vankelecom, M. A. Gilani, M. R. Bilad, Z. Sajjad and A. L. Khan, *Sep. Purif. Technol.*, 2018, **206**, 50–58.
43 H. Gong, X. Zhang, G. Wang, Y. Liu, Y. Li and Z. Jin, *Mol. Catal.*, 2020, **485**, 110832.
44 Y. Li, X. Li, H. Zhang and Q. Xiang, *Nanoscale Horiz.*, 2020, **5**, 765–786.
45 M. Gholinejad, Z. Naghshbandi and J. M. Sansano, *Appl. Organomet. Chem.*, 2020, **34**, 5522.

46 Z. Yu, L. Qian, T. Zhong, Q. Ran, J. Huang, Y. Hou, F. Li, M. Li, Q. Sun and H. Zhang, *Mol. Catal.*, 2020, **485**, 110832.
47 K. Zhao, H. Li, S. Tian, W. Yang, X. Wang, A. Pang, C. Xie and D. Zeng, *Inorg. Chem. Front.*, 2019, **6**, 715–722.
48 A. Awadallah-F, F. Hillman, S. A. Al-Muhtaseb and H.-K. Jeong, *J. Mater. Sci.*, 2018, **54**, 5513–5527.
49 Y. Wu, Z. Yue, A. Liu, P. Yang and M. Zhu, *ACS Sustainable Chem. Eng.*, 2016, **4**, 2569–2577.
50 S. Navalon, M. Alvaro and H. Garcia, *Appl. Catal., B*, 2010, **99**, 1–26.
51 X. Men, H. Chen, K. Chang, X. Fang, C. Wu, W. Qin and S. Yin, *Appl. Catal., B*, 2016, **187**, 367–374.
52 P. Zhu, X. Yin, X. Gao, G. Dong, J. Xu and C. Wang, *Chin. J. Catal.*, 2021, **42**, 175–183.
53 D. Liu, Z. Jin, H. Li and G. Lu, *Appl. Surf. Sci.*, 2017, **423**, 255–265.
54 M. Li, J. Sun, G. Chen, S. Wang and S. Yao, *Adv Powder Mater.*, 2022, **1**, 100032.